



High-resolution chemical analysis on cycled LiFePO₄ battery electrodes using energy-filtered transmission electron microscopy



Joshua D. Sugar ^{a,*}, Farid El Gabaly ^a, William C. Chueh ^d, Kyle R. Fenton ^b, Tolek Tyliszczak ^c, Paul G. Kotula ^b, Norman C. Bartelt ^a

^a Sandia National Laboratories, Livermore, CA 94550, USA

^b Sandia National Laboratories, Albuquerque, NM 87123, USA

^c Advanced Light Source, Lawrence Berkeley National Laboratory, Berkeley, CA 94720, USA

^d Materials Science and Engineering, Stanford University, Stanford, CA 94305, USA

HIGHLIGHTS

- We show a particle-arrangement-preserving method for sectioning battery electrodes.
- Energy-filtered TEM is used to map the Li distribution in half-charged electrodes.
- Our results confirm a nucleation-limited kinetic model for LiFePO₄ intercalation.

ARTICLE INFO

Article history:

Received 6 June 2013

Received in revised form

29 July 2013

Accepted 1 August 2013

Available online 13 August 2013

Keywords:

LiFePO₄

TEM

Electron energy loss spectroscopy

Phase transformation

ABSTRACT

We demonstrate an ex situ method for analyzing the chemistry of battery electrode particles after electrochemical cycling using the transmission electron microscope (TEM). The arrangement of particles during our analysis is the same as when the particles are being cycled. We start by sectioning LiFePO₄ battery electrodes using an ultramicrotome. We then show that mapping of the Fe²⁺ and Fe³⁺ oxidation state using energy-filtered TEM (EFTEM) and multivariate statistical analysis techniques can be used to determine the spatial distribution of Li in the particles. This approach is validated by comparison with scanning transmission X-ray microscopy (STXM) analysis of the same samples [Chueh et al. Nanoletters, 13 (3) (2013) 866–72]. EFTEM uses a parallel electron beam and reduces the electron-beam dose (and potential beam-induced damage) to the sample when compared to alternate techniques that use a focused probe (e.g. STEM-EELS). Our analysis confirms that under the charging conditions of the analyzed battery, mixed phase particles are rare and thus Li intercalation is limited by the nucleation of new phases.

© 2013 Elsevier B.V. All rights reserved.

1. Introduction

Modern Li-ion battery systems are complex. They contain composite electrodes with a size distribution of active particles bound together by a polymer binder in a complicated 3D microstructure [1]. The liquid electrolyte penetrates between the particles in the electrode. Particle size, porosity, and tortuosity in the electrodes are all important factors to consider when optimizing the performance and degradation of a battery [2,3]. Ultimately, understanding how the active particles are arranged in an electrode, and how each individual particle undergoes the charge/discharge reaction will yield

a fundamental understanding of the mechanisms that govern the cycle rates, power density, energy density, and efficiency of a real cycling battery. Our approach is to disassemble a cycled battery and investigate sections of the post mortem electrode particle-by-particle to understand the mechanisms that control the charge/discharge reactions. In previous work, we have relied on scanning transmission X-ray microscopy (STXM) to chemically analyze the chemical state of each particle in a LiFePO₄ electrode [4]. In this study, we show how energy-filtered TEM data can be used to probe chemical state in the same system at higher spatial resolution. The overall good agreement between the two approaches validates the Li distribution inferred from both techniques and reinforces the conclusion of the previous work: that under some conditions the charging rate of a battery can be determined by the rate of nucleation of new phases within each particle.

* Corresponding author. Tel.: +1 925 294 1344; fax: +1 925 294 3231.

E-mail address: jdsugar@sandia.gov (J.D. Sugar).

LiFePO_4 (LFP) is a well-studied battery electrode material that is attractive because of its relatively low cost, flat voltage curve at 3.5 V vs. Li/Li^+ , and ease of safe handling [5,6]. When cycled, LFP undergoes a first-order phase transformation from the Li-rich LFP phase to the Li-poor FePO_4 (FP) phase. The two phases have very limited solid solubility at room temperature, and both phases have the olivine structure with the orthorhombic unit cell [7]. There has been much work in the literature investigating the mechanism responsible for the Li-intercalation reaction in these materials and the nature of the interphase interface during the transformation [8–22]. An important question to ask is whether the rate of the LFP/FP phase transformation is limited by the motion of the interphase boundary or the nucleation of the new phase. If the phase transformation is limited by the rate at which the phase boundary moves, then it is important to differentiate cases that proceed by different mechanisms, e.g. a “core–shell” [14] or “domino-cascade” [11] model. However, if the transformation in each particle is rapid, and a “many-particle” or “mosaic” pathway [9,12,15] better describes the phase transformation, then it is far more important to understand how to increase the nucleation rate of new phases during cycling. Despite many studies, some very recent, different groups using different techniques reach contradictory conclusions as to what controls phase transformations in LFP. We next describe how the mechanisms can be differentiated by measuring the fraction of particles that are transforming at a given time. We then show the successful use of energy-filtered TEM to perform such a measurement, which unambiguously supports nucleation-limited kinetics.

A number of different micro- and macroscopic characterization techniques have been used to probe the question of how the intercalation reaction proceeds. These include X-ray and neutron diffraction [8,23–28], transmission electron microscopy (TEM) [10,13,21,29,30], electrochemical methods [31,32], and recently, X-ray absorption spectroscopy [33,34] and X-ray microscopy [4]. The high spatial resolution of the TEM has made it an attractive choice for looking at the micro and nanostructure of battery electrode materials. In fact, microscopy can distinguish between phase-boundary-migration limited and nucleation-limited kinetics without observing nucleation events or measuring the time it takes for an individual particle to change phase. The key distinguishing parameter is the fraction of particles in a mixed charge state at any particular time. To see this, consider the simplified charging history of an individual particle shown in Fig. 1. Initially the particle is uncharged. At time t_0 , the charged phase nucleates. The charged phase grows, so that the current to the particle is a constant j_0 (which, of course depends on the charging potential). The total charging time of the particle is

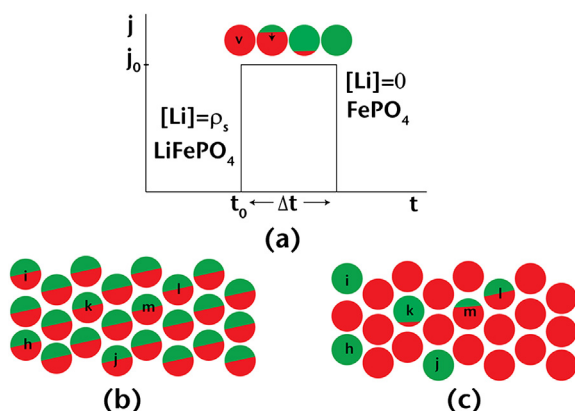


Fig. 1. (a) Schematic showing the charging of an individual LiFePO_4 particle. The fully lithiated particle has a volume, v , lithium concentration, ρ_s , and charges in time Δt . The transformation rate is limited by phase boundary migration and nucleation in (b) and (c), respectively.

$$\Delta t = \frac{\rho_s v}{j_0} \quad (1)$$

where v is the volume and ρ_s is the charge density per unit volume of the particle. If the number of charging particles N_c is comparable to the total number of particles N , then the total charging rate J will be $N_c j_0 \approx N j_0$, i.e., the total charging rate at a particular voltage will only depend on how fast the individual particles charge after nucleating a new phase (schematically shown in Fig. 1(b)). All particles are charging at the same rate. On the other hand, if the number of particles charging at any particular time is small, then

$$J = N_c j_0 = (N_u r \Delta t) j_0 = N_u r \rho_s v \quad (2)$$

where N_u is the number of untransformed particles and r is probability per unit time that the new phase nucleates. A substitution of Δt from Equation (1) into (2) removes the dependence on Δt . Thus, the charging rate, J , is determined by the nucleation rate r and independent of how fast an individual particle charges (schematically shown in Fig. 1(c)). The applied potential needed to charge the battery at some rate depends only on how the nucleation rate varies with the potential: the potential needs to be high enough to nucleate the number of charging particles per unit time required to give the specified charging rate. This model neglects such complicating effects as voltage gradients within the electrode or distributions of particle sizes. Nevertheless, determining if the fraction of particles in a mixed state of charge is small allows one to determine whether nucleation or individual particle charging rates determine the overall battery charging rate.

A number of electron microscopy-based techniques have been used to image the Li distribution in battery electrode materials. These techniques have the potential to locate and count the number of mixed-phase particles present. They include electron diffraction [10,29], electron energy loss spectroscopy [13,35–39], high-resolution TEM [21], and annular bright-field imaging [30]. For many of these techniques, it is necessary to take particles and disperse them on a TEM support grid, which destroys the native microstructure that existed in an operating battery. Our goal was to develop a technique that would allow us to observe active LFP particles in the same arrangement as they exist in a battery during cycling, and to image the distribution of Li in each particle of the electrode after the battery was cycled to a specific state of charge to determine the fraction of mixed phase particles during charging. We accomplished this using a combination of ultramicrotomy for sample preparation (see for example Ref. [40]), and energy-filtered TEM [41]. Our techniques are advantageous for two reasons. 1) The arrangement of particles in the battery is preserved during analysis because sections are microtomed from a real electrode. 2) Also, we use a parallel electron beam in energy-filtered TEM rather than a focused probe as in STEM–EELS (scanning transmission electron microscopy–electron energy loss spectroscopy), which reduces some effects of electron beam damage.

We compared our results to scanning transmission X-ray microscopy (STXM) data and found good agreement, giving us confidence in the analysis. Ultimately, our ex situ forensic analysis on LFP electrodes under the charging conditions of this study suggests that the nucleation of new phases is the most important rate-determining step in the phase transformation.

2. Experimental procedures

2.1. Electrochemical cycling

Standard coin-cell geometry batteries were prepared with a Li anode and an approximate 35- μm thick carbon-coated LFP/graphite/PVDF composite cathode. The average LFP particle size

was ~ 220 nm, and in general, each particle of LFP is a single crystal. The electrolyte was 1.2 M LiPF₆/ethylene carbonate (EC)/ethyl methyl carbonate (EMC) with a 3:7 weight ratio of EC:EMC. The battery was electrochemically cycled five times to obtain a stable capacity of 150 mA h g⁻¹. We then charged a battery at a rate of 1 C–75 mA h g⁻¹ (50% state of charge). Electrochemical data can be found in the supplemental information of Ref. [4]. After reaching the desired state of charge, the cell was rapidly disassembled and rinsed with excess dimethyl carbonate in a dry room. The disassembly procedure was completed within 4 min of terminating the charge, which is faster than typical voltage relaxation times [42,43]. The LFP particles are mostly not in contact with one another after the electrolyte is removed [1], which prevents further Li redistribution after disassembly. It is possible, however, for Li to redistribute within a single particle, however, we will show that very few of the particles we measured exhibit two-phase coexistence within a single particle.

2.2. Transmission electron microscopy

After the battery coin cells were disassembled, the LFP electrodes were removed. Two methods were used to examine individual particles of LFP by TEM after being electrochemically cycled in the coin cell. In the first method, LFP particles were scraped from the electrode with a razor blade. These particles were dispersed in ethanol and ultrasonicated for approximately 1 h. The particles were pipetted onto a Cu TEM support grid (Ted Pella Inc.). For the second method, a small piece of the electrode was cross-sectioned into electron transparent slices using the ultramicrotome (Leica EM UC7). The ultramicrotome produced thin slices across the entire width of the electrode. The operation of the ultramicrotome to produce thin cross sections is shown schematically in Fig. 2(a). Slices of electrode are made in which the arrangement of active LFP particles in each slice is not disturbed relative to their arrangement in the coin cell. The thin cross-sections spanned the entire width of the electrode from the electrode/electrolyte interface to the current collector interface. An optical micrograph of a cross section prepared with the ultramicrotome is shown in Fig. 2(b). The entire 35-μm thick LFP electrode is visible, and a portion of the Al current collector has delaminated from the electrode during the sectioning.

Transmission electron microscopy was performed using a JEOL 2010F operating at 200 kV equipped with a Gatan 860 GIF EELS spectrometer. In addition to imaging the particles, EELS (electron energy loss spectroscopy) spectrum imaging was performed in which an EELS spectrum is recorded at each pixel of an image. Two acquisition techniques were used to collect EELS spectrum images and these are depicted in Fig. 3. In Fig. 3(a), a focused STEM (scanning transmission electron microscopy) probe is used to collect an EELS spectrum at each pixel. One spectrum is collected, the probe is moved, and then the next spectrum is collected. The other technique, EFTEM (energy-filtered TEM)-spectrum imaging, is shown in Fig. 3(b). This technique utilizes a conventional, parallel electron beam and collects an image at a particular energy loss with an energy-selecting slit. Then, the energy-selecting slit is moved an energy, ΔE , and another image is collected. In this way, an EELS spectrum is constructed at each pixel, and the same information can be collected as in the STEM–EELS case. We collected data with an energy slit width of 5 eV and a ΔE of 1 eV for each energy plane. Usually, there are more data artifacts introduced with EFTEM data collection than STEM–EELS. These artifacts cannot be corrected during acquisition easily (e.g. dark current drift, ghosting on the CCD, spatial drift, energy drift). We collected our data with the SmartEFTEM acquisition package [44], which eliminated many issues associated the CCD during data collection.

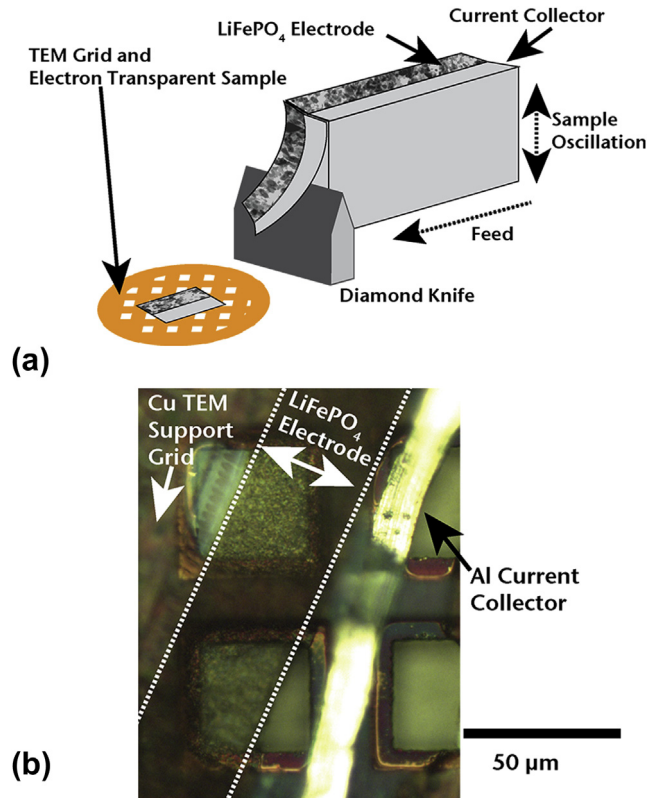


Fig. 2. (a) Schematic showing the operation of a microtome to fabricate cross sections of battery electrodes. The cross sections are electron transparent, and they span the full width of the battery electrode. An optical micrograph of a battery cross section is shown in (b). The current collector has delaminated from the electrode during sectioning. The electrode spans across holes in the TEM support grid, where the TEM can resolve each individual particle.

2.3. Data processing and analysis

Several artifacts are introduced during EFTEM-SI data acquisition that must be corrected for such as non-isochromaticity, spatial drift, and energy drift. Correction of these artifacts post-acquisition

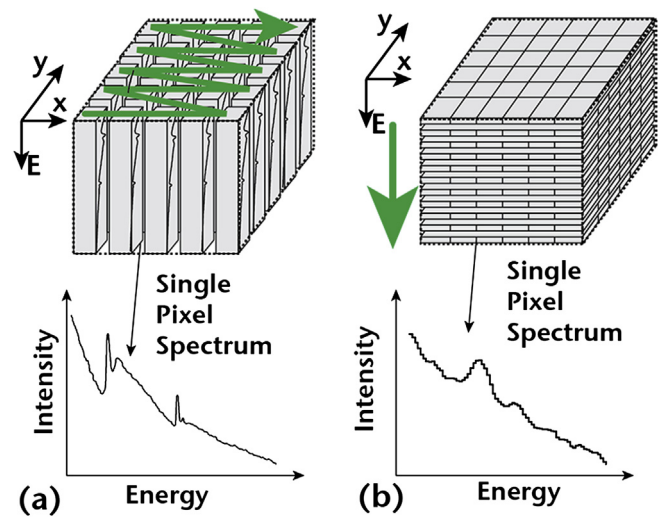


Fig. 3. A schematic illustrating the difference between STEM–EELS (a) and EFTEM (b) spectrum imaging. For STEM–EELS, a focused STEM probe is scanned across a region of the sample and EELS spectra are collected at each pixel. EFTEM spectrum image data is collected with a parallel electron beam, and images are acquired of each energy plane. The end result in both cases is data at each (x , y , energy) triplet.

is described in detail in the literature [45]. We corrected for non-isochromaticity using the position of the zero-loss peak, and we used the freely available SDSD correction for spatial drift [46]. We did not correct for energy drift because we determined that the total energy drift during acquisition was much smaller than the width of the energy-selecting slit (5 eV), and therefore it would not make a significant difference in the data analysis.

To determine the Li distribution from EFTEM-SI data, we examined the state of charge of the Fe from the EELS spectra. The literature has shown that the position of the Fe L edge shifts by approximately 2 eV when Fe changes from Fe^{2+} in LiFePO_4 to Fe^{3+} in FePO_4 [13]. This shift is difficult to measure with EFTEM-SI because the width of the energy-selecting slit is 5 eV and a typical energy resolution of the EELS spectrometer (FWHM of the zero-loss peak) is 1.5 eV. While it is still possible to measure the Fe L edge shift, this task was made easier by our use of multivariate statistical analysis (MSA) techniques. MSA describes a series of mathematical techniques used for matrix decomposition and is commonly used in analytical electron microscopy [47–49]. A spectrum image data cube, D , of p channels and dimensions ($x \cdot y$) can be represented by the more compact form:

$$D \approx C \cdot S \quad (3)$$

where C is a matrix of spatial pixel weightings of dimension $(x \cdot y) \cdot n$, and S represents the $p \cdot n$ matrix of “pure” component spectra. This technique assumes that the data follows a linear additive model. C and S can be calculated from a variety of MSA techniques including principal component analysis (PCA), singular value decomposition (SVD), and multivariate curve resolution (MCR). MCR has been shown to be successful in the analysis X-ray absorption spectra from battery electrode materials [50].

We used a “spatially simple” multivariate curve resolution algorithm developed at Sandia (AXSIA) that has been described in detail in the literature [47,48,51–55]. The results of the MSA analysis yielded pure spectral components that corresponded to the Fe^{2+} and the Fe^{3+} states in addition to other carbon and spectral background components. Reference spectra for the pure Fe^{2+} and Fe^{3+} states could be extracted from the raw data by locating the most intense pixels of the pure components in the MSA analysis. These reference spectra were also used for multiple linear least squares (MLLS) fitting to map the Fe state of charge in an area of the sample. MLLS also solves Equation (3), but instead of calculating S from MSA, the spectra used in S are specified by the user and are extracted directly from the data or selected from a library of reference spectra. Then, a simple matrix division solves for the coefficients in C . The Fe state-of-charge map was determined by:

$$\text{Fe state of charge} = \frac{I_{\text{FePO}_4}}{I_{\text{LiFePO}_4} + I_{\text{FePO}_4}} \quad (4)$$

where the intensities, I_{LiFePO_4} and I_{FePO_4} , are determined by the coefficients in C of the MLLS fit. When the Fe state-of-charge is calculated to be 0 at a particular pixel, the Fe is in the Fe^{2+} state and Li is present, when it is 1, it is Fe^{3+} . The determination of the Li distribution after cycling of the LFP electrode material allowed us to learn about the mechanisms of the phase transformation during electrochemical cycling.

3. Results

The first step in determining the Li distribution in cycled battery electrode material was to determine the spectral reference shapes for Fe^{2+} in LiFePO_4 and Fe^{3+} in FePO_4 . It is well known from the literature that our monochromated system can easily differentiate

between the two spectral shapes [13]. It was not clear that a non-monochromated system would be able to differentiate so easily because the energy resolution (~ 1.5 eV) is roughly the same as the Fe L edge shift. Reference shapes for FePO_4 was determined in two ways: 1) The chemical delithiation of LiFePO_4 by soaking in a solution of NO_2BF_4 in acetonitrile, and 2) the electrochemical delithiation of LiFePO_4 using a coin cell as described in the Experimental procedures above. The resulting EELS spectra for both experiments is shown in Fig. 4(a) and (b).

Regardless of whether the FePO_4 is prepared by chemical delithiation or electrochemical delithiation, the spectra show a shift 1.5–2 eV for the peak position of the Fe L3 edge. This peak shift is observable in our non-monochromated system, which is somewhat surprising because the energy resolution measured by the FWHM of the zero-loss peak is typically approximately 1.5 eV. However, these spectra show that it is possible to use STEM–EELS to map the Fe state-of-charge. Unfortunately, the use of a focused electron probe in STEM mode causes beam damage that ultimately limits the usability of STEM.

The effects of beam damage are shown in Fig. 4(c). Here, a STEM-probe was kept stationary on a single FePO_4 particle and an EELS spectrum was recorded every second (with a 1 s exposure) for 50 s. There are two visible artifacts that result from beam damage. The HAADF image shows a small hole in the particle at the location of the focused electron beam (marked with an arrow). So, the focused electron beam has removed material and caused a large decrease in the available signal for EELS as shown by the difference in the EELS intensities. Also, there is a visible shift in the position of the Fe L3 edge of 1 eV, where the last spectrum recorded has a peak position 1 eV lower than the first spectrum. This is consistent with the beam-induced reduction of Fe from Fe^{3+} to Fe^{2+} and evidence in the literature that the electron beam can cause the reduction of Fe ions [56]. Electron-beam induced reduction of cations is a common occurrence in the electron microscope [57,58].

While it is unlikely that one would need a 50 s exposure to measure Fe EELS spectra during a spectrum image, this time is used to illustrate the extreme case, the onset of beam-induced Fe reduction can occur at much shorter times. The results of Pan et al. [56] suggest that lowering the accelerating voltage of the microscope to 100 kV has the potential to slow the damage, however, it is unclear whether the damage is caused by direct atomic displacement or secondary events. Even if the primary electron beam energy is reduced, it may be necessary to increase the acquisition time for high quality spectra. Since the total electron fluence (electrons/ nm^{-2}) determines the onset of electron-beam induced Fe reduction, lowering the beam energy might not prevent sample damage. Therefore, the use of STEM–EELS for mapping the Fe state-of-charge in LiFePO_4 -based materials will be limited, particularly in our characterization system because the measurement itself could change the Fe state of charge. Therefore, we determined that EFTEM-SI would be a more successful approach because one can spread the beam to a larger area, greatly decreasing the electron dose to the area of interest and minimizing the effects of beam-induced artifacts.

The use of EFTEM-SI and MSA to determine the Fe state of charge is shown in Fig. 5. A zero-loss image of LiFePO_4 particles electrochemically charged to 50% state of charge and distributed on a Si_3N_4 support grid is shown in Fig. 5(a). The score plot used to generate the number of principal components is shown in Fig. 5(b). The first 5 components deviate significantly from the linear fit to the random noise components (component #6 and above). The “score” (pixel weighting) images for component #2 and component #4 show that these correspond to the Si_3N_4 support that holds the particles. The spectra and score images for components # 1, 3, and 5 are shown in Fig. 5(c). The spectra for component #3 and #5 show a

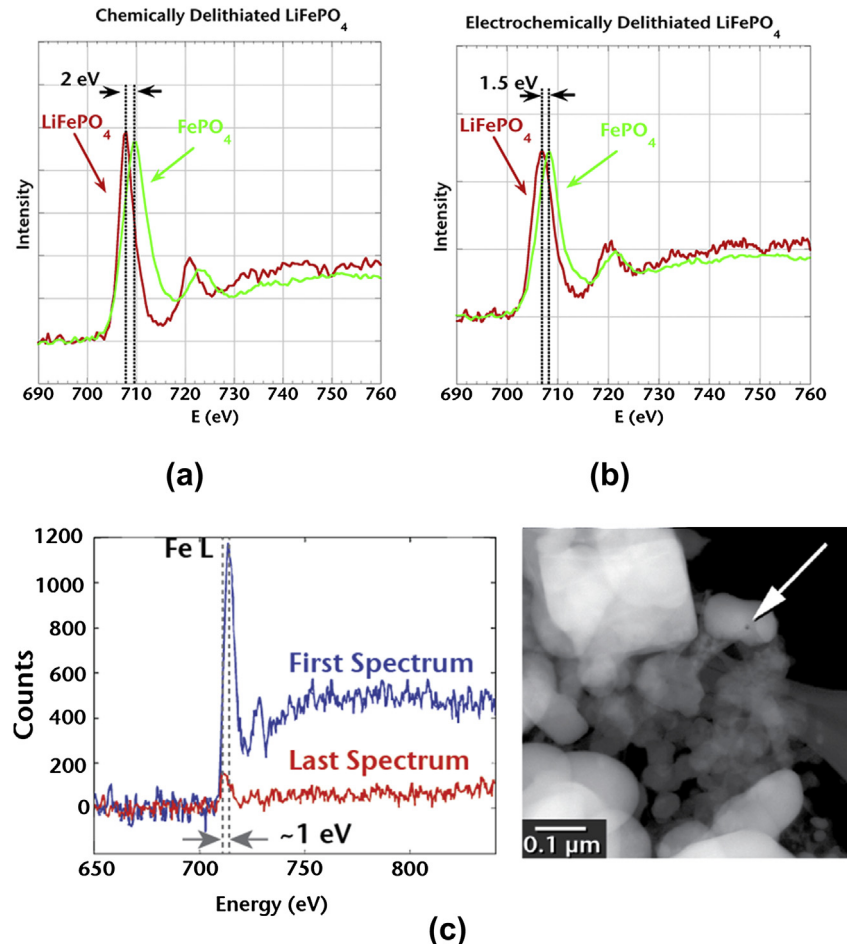


Fig. 4. EELS spectra from reference materials of LiFePO₄ and FePO₄ prepared by (a) chemical delithiation of LiFePO₄ in NO₂BF₄, and (b) electrochemical delithiation of LiFePO₄ in a battery coin cell. In (c), the results of collecting an EELS spectrum every second for 50 s is shown. There is a reduction in the Fe L edge intensity and a shift of the peak position consistent with the reduction of Fe. The HAADF STEM image shows that the focused electron beam has removed material and made a hole (marked with arrow).

shift in the Fe L3 edge of approximately 3 eV. Although the detailed fine structure differences (e.g. Ref. [13]) are not visible with an energy step of 1 eV in the EFTEM spectra, the observed peak shift is consistent with the observed shift in position of the Fe L3 edge when Fe changes from a 3+ to 2+ oxidation state. Therefore, components #3 and #5 are consistent with LiFePO₄ and FePO₄, respectively. Component #1 causes most of the centers of the particles to light up, and since most of these particles are round, we expect them to be thicker in the middle. The thickness map is also consistent with component #1 identifying regions where the relative thickness (t/λ) is greater than approximately 1.5. Therefore, component #1 is identifying sample region that is thick, which causes non-linear effects in the spectra and a peak position of the L3 edge that is mixed between the apparent position for 2+ and 3+ Fe. When samples are thick, plural scattering occurs and causes a redistribution of intensity to higher energy losses [59–61]. This effect can cause the apparent mixing of Fe²⁺ and Fe³⁺ states in the fitting because intensity is artificially higher at energies between the L3 edge peak intensities for the Fe²⁺ and Fe³⁺ reference states.

The EFTEM-SI measurements of Fe oxidation state were validated by a comparison with measurements obtained using scanning transmission X-ray microscopy (STXM). Ultimately, it was desired to validate the results of the EFTEM-SI data with another measurement of Fe oxidation state. STXM spectra are similar to EELS spectra in that they both measure absorption of the incoming illumination by the sample. However, STXM uses illumination generated from a synchrotron X-ray source (Advanced Light Source

at LBNL), while EELS uses electron illumination in the TEM. The advantages of the STXM are the increased energy resolution and decreased sensitivity of the sample to X-ray beam damage, but the spatial resolution of STXM is only ~ 30 nm, much less than what is possible in the TEM. Fig. 6 shows the same particles supported on a Si₃N₄ grid measured with both STXM and TEM. The details of the STXM can be found in Ref. [4]. It is much easier to identify the individual particle boundaries and when particles overlap in the TEM zero-loss image, illustrating the higher spatial resolution of the TEM.

The Fe state-of-charge map in Fig. 6 is shown in two ways that can be compared to the STXM data. Both the output of the MSA analysis (similar to Fig. 5) and the Fe state of charge calculated by MLLS (Equation (4)) is shown and both are relatively consistent with the STXM state-of-charge map. The MSA output shows regions that are mostly red and mostly green, and these regions are consistent with the red and green locations in the STXM data. However, the particle centers are not identified as either red or green in the MSA output because plural scattering and non-linear thickness effects create another component for thicker regions (as seen in Fig. 5). Also, the MLLS calculation results in many of the particle centers being yellow (a linear combination of the red 2+ and green 3+ states). This is also caused by plural scattering and non-linear thickness effects in the EELS spectra. In order to obtain better Fe state-of-charge maps with fewer artifacts from the non-linear thickness effects, we prepared samples with the ultramicrotome. This results in samples with a more uniform thickness

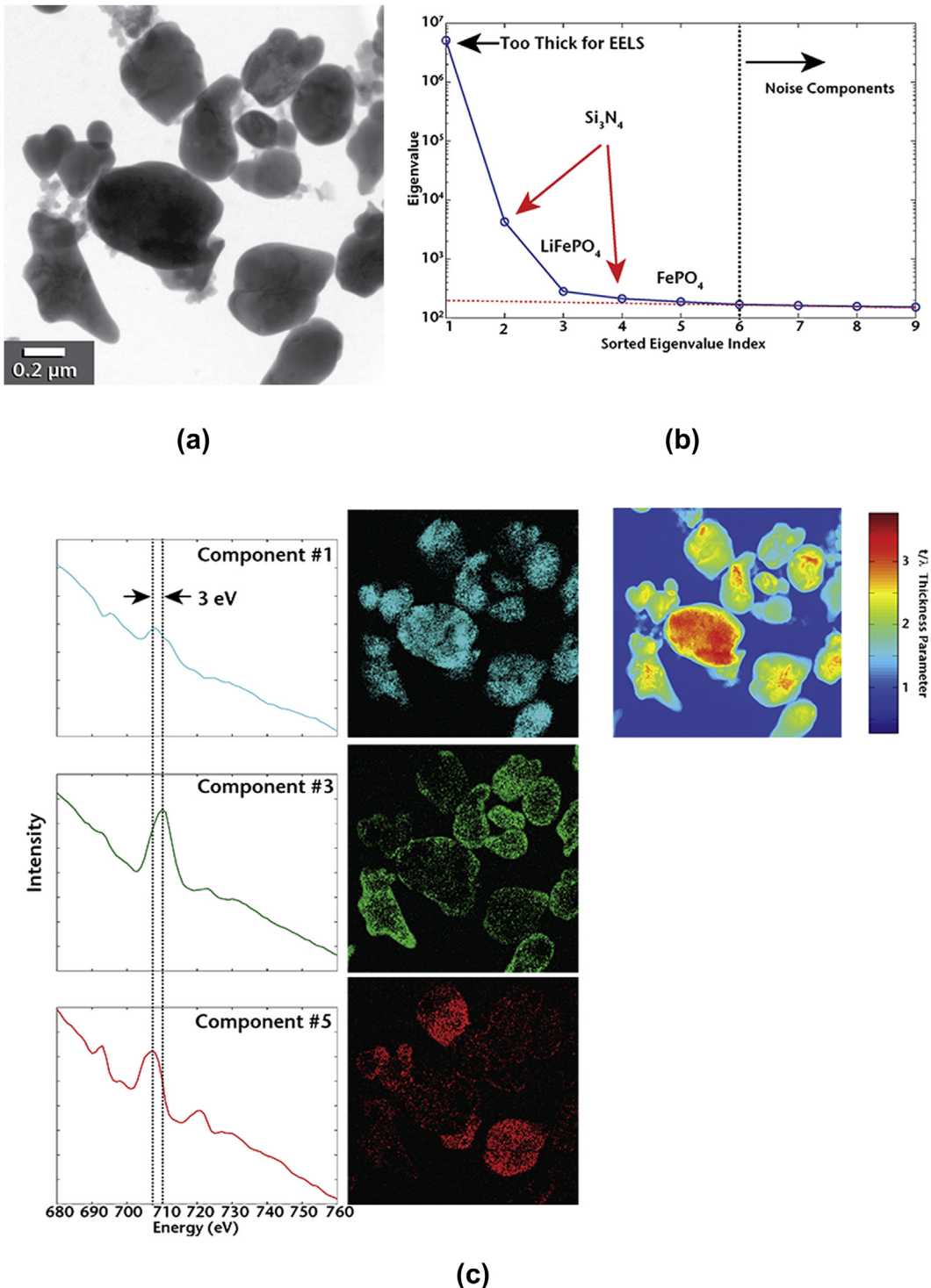


Fig. 5. (a) Zero-loss image of 50% state of charge particles on a Si_3N_4 support grid. (b) Scree plot generated by spatial simplicity MCR decomposition of the EFTEM data set. The pure component spectra (loadings) and their corresponding score images are shown in (c) for components 1,3, and 5. These components correspond to particles and are consistent with LiFePO_4 in component 5, FePO_4 in component 3, and thick material in which non-linear thickness effects dominate in component 1.

across the sample and fewer thick regions that have harder to interpret EELS spectra.

Fig. 7 shows that when EFTEM-SI analysis is performed on ultramicrotomed samples, there is good agreement with the STXM data and fewer thickness artifacts are observed. A comparison is shown for three sample regions. In each region, the Fe state of charge is measured with both STXM and EFTEM-SI. The zero-loss

TEM images in Fig. 7(a) show that the spatial resolution of the TEM is sufficient to determine when particles overlap. Fig. 7(b) shows the STXM maps of the Fe oxidation state. In the STXM maps, regions yellow in color suggest that the Fe has a mixed oxidation state. It is not possible to tell from the STXM data alone whether the mixed oxidation state occurs because an individual particle has both the LiFePO_4 and FePO_4 phases, or because two particles with

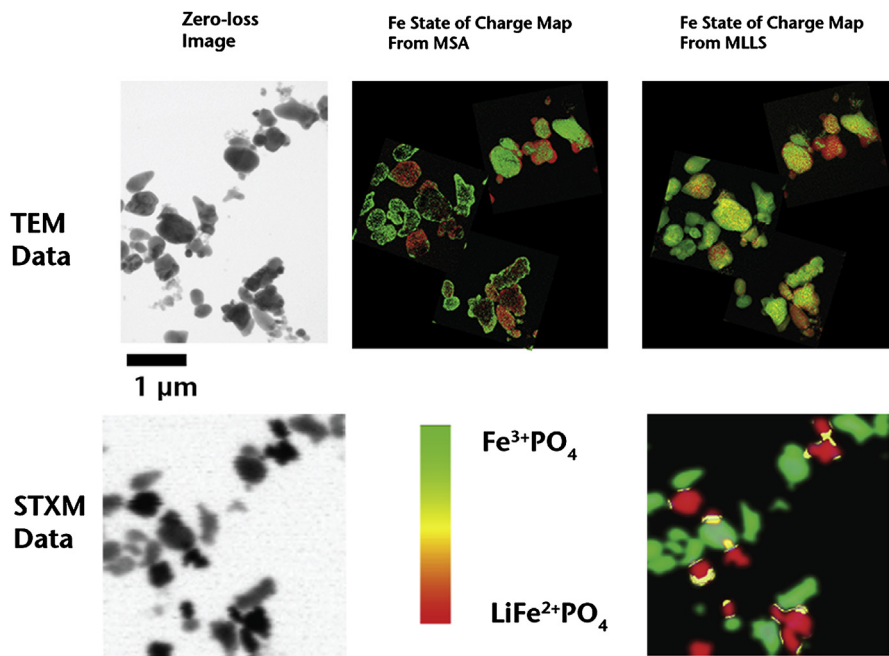


Fig. 6. Comparison of EFTEM and STXM data for LiFePO_4 particles suspended on a Si_3N_4 support film. A comparison of the TEM MSA results and the STXM results show that the red regions and green regions are identical. The non-linear thickness effects cause the MLLS analysis on the EFTEM data to have more yellow than the STXM data. (For interpretation of the references to color in this figure legend, the reader is referred to the web version of this article.)

different oxidation states are overlapping each other. The TEM data allows us to more easily discern when particle overlap is occurring.

The results of the TEM analysis suggest that the particles are generally either in a Fe^{2+} or a Fe^{3+} state with mixed oxidation states only occurring when there is significant particle overlap. The results of MSA calculation are shown in Fig. 7(c). Here, only the components for the pure Fe^{2+} (red) and Fe^{3+} (green) are shown, the components for the C support and background have been omitted. There are still some particles that are black in the center because of thickness effects, but the MSA allows us to clearly identify regions that exhibit the two different oxidation states as shown by the ~ 1.5 eV shift of the Fe L3 edge in the component spectra. The MSA data is used to identify the most intense pixels for the Fe^{2+} and Fe^{3+} states. Then, spectra from these regions are used as reference shapes in the MLLS fit to create the Fe state map (Equation (4)) in Fig. 7(d). A comparison of the STXM maps in Fig. 7(b) and the Fe maps determined from MLLS in Fig. 7(d) are generally in good agreement. That two such different analysis techniques give the same result gives considerable confidence that the charge maps are correct.

4. Discussion

As described in the introduction, to answer the question of whether charging is determined by nucleation or individual particle charging (phase boundary migration) rates one needs to determine the fraction of mixed phase particles at any time. The main experimental difficulty in doing this is to determine whether the “yellow” regions in Fig. 7 correspond to phase boundaries in individual particles or whether they are created by overlap between two independent particles. Consistent with the STXM chemical analysis, the results of the EFTEM analysis suggest that particles are rarely in a mixed state of charge. Indeed, the high-spatial resolution of the TEM allows us to definitively determine that many particles with a mixed state of charge appearance are actually overlapping other particles in the projected view. We now discuss some of the subtleties associated with this determination

and how high-resolution data and the combination of EFTEM and STXM can be useful in resolving them.

Three regions in Fig. 7(d) have been marked (**a**, **b**, and **c**) for further investigation. In **a** it is ambiguous whether there are two overlapping particles or a single particle that exhibits both Fe states. A higher-magnification view of this region is shown in Fig. 8(a). The particle edges have been outlined for clarity with a white dotted line. This image shows that overlapping particles causes the appearance of mixed Fe states in the projection view. Similarly, in Fig. 8(b), there are several overlapping particles, and the STXM data does not show one of the green particles. The spatial resolution of the STXM makes it difficult to discern particle boundaries, and this particle could be too thin to give a sufficient STXM signal. It is possible that the red region seen in STXM is entirely due to the overlapping red particle seen in EFTEM. Thus there is no conclusive evidence for a mixed phase particle in this region.

The situation in Fig. 8(c) is more complicated. In EFTEM, there are two central particles that show a significant amount of mixed phase character. The particle in the lower left is red on the right and transitions to green on the left. The BF TEM reveals that a small particle, circled in the image, overlaps the upper right portion of the large particle. This overlap is likely the cause of the mixed phase character in this lower particle. The large upper particle overlaps other particles and contains a fairly high mixed charge component (yellow) distributed uniformly throughout the particle in EFTEM, while STXM suggests a phase boundary on the upper right of the particle. A measurement of the relative thickness of this particle with EELS shows that t/λ is as high as 2.5. Since this particle is particularly thick, it is possible that non-linear thickness effects on the EELS spectra due to plural scattering cause the spurious appearance of mixed states of charge as discussed above. Another possibility is that the particle has rotated slightly between the STXM and EFTEM measurements. Then, the “red” charged region detected by STXM could be underneath the “green” region causing “yellow” in the projected view of the EFTEM state of charge map. Certainly, STXM is less sensitive to thickness effects than TEM and is

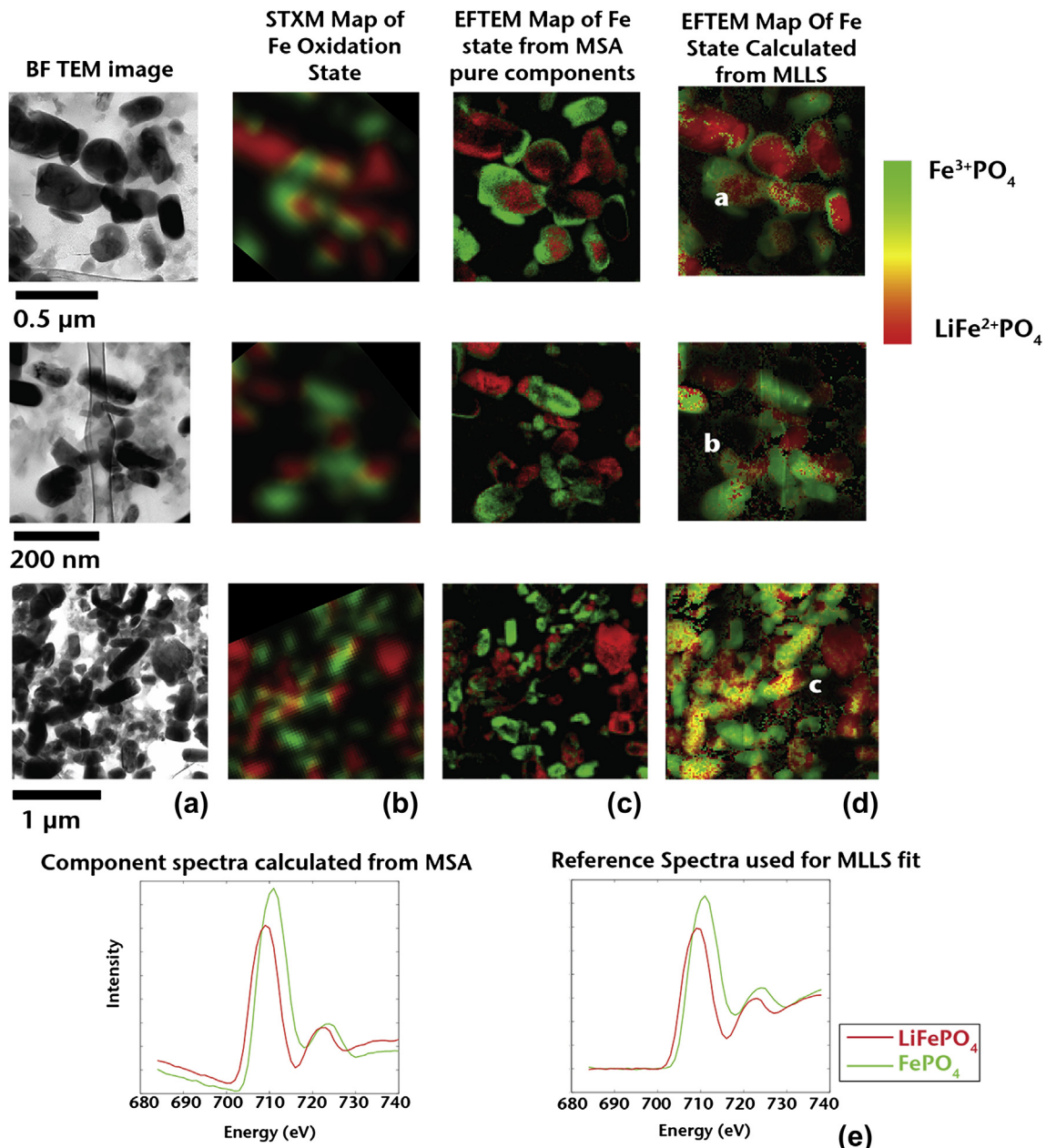


Fig. 7. Comparison of EFTEM and STXM Fe state-of-charge mapping. Bright-field images of electrode particles are shown in (a). The Fe oxidation state measured from STXM is shown in (b). This is compared to the Fe state measured by EFTEM in (c) and (d). In (c), the LFP and FP components of the MSA analysis are mapped. Good agreement is found when compared to the STXM data. In (d), intense LFP and FP regions are identified from (c), and reference spectra shapes are extracted and used to perform the MLLS fit in (d). Typical spectral shapes for the two techniques are shown in (e). (For interpretation of the references to color in this figure legend, the reader is referred to the web version of this article.)

less likely to have the artificial appearance of mixed phase particles, but STXM cannot discern the particle boundaries easily at diameters of ~ 220 nm. Despite these subtle differences in the state of charge maps, the general conclusion that a small fraction of total particles is actively charging at a given time is supported by the results of both techniques. It is clear that a combination of the two techniques provides more information and confidence for mapping charge states and is better than one measurement alone.

Analysis of a large number of particles in the STXM for which there was little ambiguity about particle overlap from the same sample shows that particles exhibit both Fe oxidation states only approximately 2% of the time [4]. The other 98% are either completely Fe^{2+} or Fe^{3+} . Mixed phase particles are certainly rare. A

recent study using in situ X-ray measurements found that during the intercalation reaction LFP and FP particles exist with a Li composition within the miscibility gap [22,62]. This measurement confirms that nucleation is a critical rate-limiting step in the reaction because the existence of metastable states implies the difficulty of nucleation. Such a measurement on ensembles of particles sheds insight into the nucleation process itself, however, to be more quantitative about exactly how many particles are in a mixed state of charge requires a particle-by-particle measurement with careful analysis of particle boundaries at high spatial resolution. Then, particle overlap can be identified. This is not possible to infer from STXM data alone, and requires a high-resolution technique like we show here with the TEM. The motivation for such an

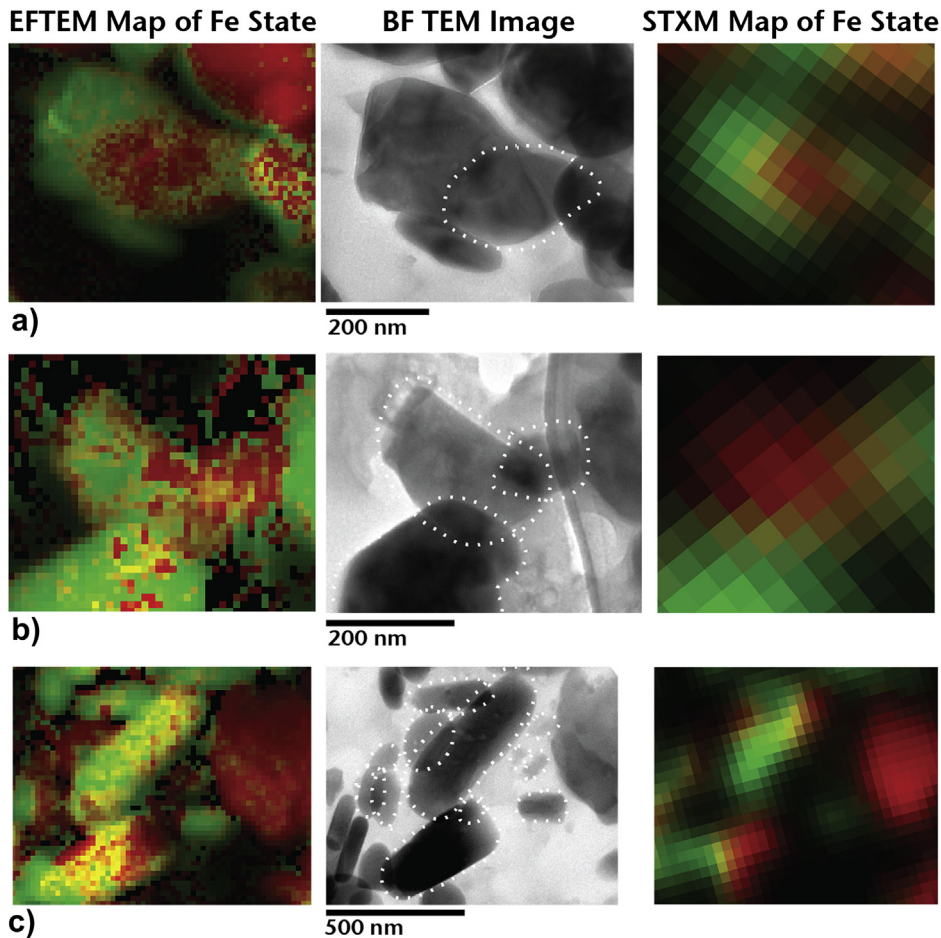


Fig. 8. High-magnification views of regions marked a, b, and c in Fig. 7(d) with corresponding bright-field (BF) TEM images. Some particle boundaries are outlined in the BF TEM images for clarity. Close inspection shows that for these particles, mixing of Fe^{2+} and Fe^{3+} can be explained as a result of overlapping particles in projection. In general, we do not observe particles exhibiting multiple states of charge. Some of the subtleties of interpretation are discussed in the text.

analysis is that the fraction of particles that are in the process of transforming is

$$\frac{N_c}{N_u} = \frac{J}{j_0} = \left(\frac{r}{j_0} \right) \rho_s v \quad (5)$$

Since it depends on both the particle charging current, j_0 , and the nucleation rate, r , it provides a method of showing how relative changes in nucleation vs. growth rates change with charging conditions.

5. Conclusions

In this study, we have demonstrated a number of experimental techniques that shed insight on the phase transformation mechanisms active during LiFePO_4 -battery cycling. We describe a method of sectioning electrodes for high-spatial resolution morphological and chemical analysis, which has significant advantages. We also show that the combination of energy-filtered TEM and data processing routines that include multivariate statistical analysis and multiple least squares fitting can be used to give state-of-charge maps for LiFePO_4 electrode particles. The results are compared to results from the STXM and are in good agreement, validating both approaches. The good agreement between both datasets suggests that it is possible to obtain the needed information from the TEM. Since TEM is more widely available than STXM, EFTEM presents a convenient way to probe nanoscale chemistry in battery electrodes.

Finally, our results reaffirm the findings Brunetti et al. [29] and Chueh et al. [4] that a small fraction of mixed phase particles exist. Brunetti et al. concluded that this result provides support for the “domino-cascade” mechanism. For the charging conditions of the batteries examined in these studies, the actual transformation of an individual particle happens very fast relative to the time it takes to charge a battery. Therefore, whether the particle transforms via a “domino-cascade” mechanism or a “core–shell” mechanism is irrelevant to optimizing performance. The important point is the time it takes for the new phase to nucleate. Because smaller particles are more likely to nucleate the new phase [4], electrodes with a smaller average LiFePO_4 particle size may have improved performance. Alternatively, some other means of reducing the nucleation barrier such as introducing heterogeneous nucleation sites may improve performance.

Acknowledgments

Special thanks to Mark Homer, Ray Tweten, Masashi Watanabe, Bernhard Schaffer, Kevin McCarty, Tony McDaniel, and Helmut Gnaegi. The research was supported by the U.S. Department of Energy through the Sandia Laboratory Directed research and Development program. F.E.G. and N.C.B. acknowledge support from the Office of Basic Energy Science, Division of Materials Sciences and Engineering. The Advanced Light Source is supported by the Director, Office of Science, Office of Basic Energy Sciences, of the

U.S. Department of Energy under Contract No. DE-AC02-05CH11231. Sandia National Laboratories is a multi-program laboratory managed and operated by Sandia Corporation, a wholly owned subsidiary of Lockheed Martin Corporation, for the U.S. Department of Energy's National Nuclear Security Administration under contract DE-AC04-94AL85000.

References

- [1] M. Ender, J. Joos, T. Carraro, E. Ivers-Tiffee, *Electrochem. Commun.* 13 (2011) 166–168.
- [2] Y. Qi, S.J. Harris, *J. Electrochem. Soc.* 157 (2010) A741–A747.
- [3] P.R. Shearing, N.P. Brandon, J. Gelb, R. Bradley, P.J. Withers, A.J. Marquis, S. Cooper, S.J. Harris, *J. Electrochem. Soc.* 159 (2012) A1023–A1027.
- [4] W.C. Chueh, F. El Gabaly, J.D. Sugar, N.C. Bartelt, A.H. McDaniel, K.R. Fenton, K.R. Zavadil, T. Tyliszczak, W. Lai, K.F. McCarty, *Nano Lett.* 13 (2013) 866–872.
- [5] A.K. Padhi, K.S. Nanjundaswamy, J.B. Goodenough, *J. Electrochem. Soc.* 144 (1997) 1188–1194.
- [6] A.K. Padhi, K.S. Nanjundaswamy, C. Masquelier, S. Okada, J.B. Goodenough, *J. Electrochem. Soc.* 144 (1997) 1609–1613.
- [7] M. Tang, W.C. Carter, Y.-M. Chiang, *Annu. Rev. Mater. Res.* 40 (2010) 501–529.
- [8] A.S. Andersson, B. Kalska, L. Häggström, J.O. Thomas, *Solid State Ionics* 130 (2000) 41–52.
- [9] A.S. Andersson, J.O. Thomas, *J. Power Sources* 97–8 (2001) 498–502.
- [10] G.Y. Chen, X.Y. Song, T.J. Richardson, *Electrochem. Solid State Lett.* 9 (2006) A295–A298.
- [11] C. Delmas, M. Maccario, L. Croguennec, F. Le Cras, F. Weill, *Nat. Mater.* 7 (2008) 665–671.
- [12] W. Dreyer, J. Jamnik, C. Gahlke, R. Huth, J. Moskon, M. Gaberscek, *Nat. Mater.* 9 (2010) 448–453.
- [13] L. Laffont, C. Delacourt, P. Gibot, M.Y. Wu, P. Kooyman, C. Masquelier, J.M. Tarascon, *Chem. Mater.* 18 (2006) 5520–5529.
- [14] V. Srinivasan, J. Newman, *J. Electrochem. Soc.* 151 (2004) A1517–A1529.
- [15] R. Malik, F. Zhou, G. Ceder, *Nat. Mater.* 10 (2011) 587–590.
- [16] N. Meethong, H.Y.S. Huang, S.A. Speakman, W.C. Carter, Y.M. Chiang, *Adv. Funct. Mater.* 17 (2007) 1115–1123.
- [17] A. Van der Ven, K. Garikipati, S. Kim, M. Wagemaker, *J. Electrochem. Soc.* 156 (2009) A949–A957.
- [18] A. Van der Ven, M. Wagemaker, *Electrochem. Commun.* 11 (2009) 881–884.
- [19] M. Wagemaker, F.M. Mulder, A. Van der Ven, *Adv. Mater. (Weinheim, Ger.)* 21 (2009) 2703–2709.
- [20] P. Gibot, M. Casas-Cabanas, L. Laffont, S. Levasseur, P. Carlach, S. Hamelet, J.M. Tarascon, C. Masquelier, *Nat. Mater.* 7 (2008) 741–747.
- [21] C.V. Ramaña, A. Mauger, F. Gendron, C.M. Julien, K. Zaghib, *J. Power Sources* 187 (2009) 555–564.
- [22] Y. Oriksa, T. Maeda, Y. Koyama, H. Murayama, K. Fukuda, H. Tanida, H. Arai, E. Matsubara, Y. Uchimoto, Z. Ogumi, *Chem. Mater.* 25 (2013) 1032–1039.
- [23] S.P. Badi, M. Wagemaker, B.L. Ellis, D.P. Singh, W.J.H. Borghols, W.H. Kan, D.H. Ryan, F.M. Mulder, L.F. Nazar, *J. Mater. Chem.* 21 (2011) 10085–10093.
- [24] J.L. Jones, J.T. Hung, Y.S. Meng, *J. Power Sources* 189 (2009) 702–705.
- [25] Y.H. Kao, M. Tang, N. Meethong, J.M. Bai, W.C. Carter, Y.M. Chiang, *Chem. Mater.* 22 (2010) 5845–5855.
- [26] N. Meethong, Y.H. Kao, M. Tang, H.Y. Huang, W.C. Carter, Y.M. Chiang, *Chem. Mater.* 20 (2008) 6189–6198.
- [27] N. Sharma, X.W. Guo, G.D. Du, Z.P. Guo, J.Z. Wang, Z.X. Wang, V.K. Peterson, *J. Am. Chem. Soc.* 134 (2012) 7867–7873.
- [28] J. Liu, M. Kunz, K. Chen, N. Tamura, T.J. Richardson, *J. Phys. Chem. Lett.* 1 (2010) 2120–2123.
- [29] G. Brunetti, D. Robert, P. Bayle-Guillemaud, J.L. Rouviere, E.F. Rauch, J.F. Martin, J.F. Colin, F. Bertin, C. Cayron, *Chem. Mater.* 23 (2011) 4515–4524.
- [30] L. Gu, C. Zhu, H. Li, Y. Yu, C. Li, S. Tsukimoto, J. Maier, Y. Ikuhara, *J. Am. Chem. Soc.* 133 (2011) 4661–4663.
- [31] J.L. Allen, T.R. Jow, J. Wolfenstine, *Chem. Mater.* 19 (2007) 2108–2111.
- [32] G. Oyama, Y. Yamada, R. Natsui, S. Nishimura, A. Yamada, *J. Phys. Chem. C* 116 (2012) 7306–7311.
- [33] G. Ouvrard, M. Zerrouki, P. Soudan, B. Lestriez, C. Masquelier, M. Morcrette, S. Hamelet, S. Belin, A.M. Flank, F. Baudelet, *J. Power Sources* 229 (2013) 16–21.
- [34] M. Giorgetti, *ISRN Mater. Sci.* 2013 (2013) 22, Article ID 938625.
- [35] F. Cosandey, D. Su, M. Sina, N. Pereira, G.G. Amatucci, *Micron* 43 (2012) 22–29.
- [36] P. Moreau, *Appl. Phys. Lett.* 94 (2009) 123111.
- [37] J. Graetz, A. Hightower, C.C. Ahn, R. Yazami, P. Rez, B. Fultz, *J. Phys. Chem. B* 106 (2002) 1286–1289.
- [38] Y.S. Meng, T. McGilvray, M.-C. Yang, D. Gostovic, F. Wang, D. Zeng, Y. Zhu, J. Graetz, *Electrochem. Soc. Interface* 20 (2011) 49–53.
- [39] F. Wang, H.-C. Yu, M.-H. Chen, L. Wu, N. Pereira, K. Thornton, A. Van der Ven, Y. Zhu, G.G. Amatucci, J. Graetz, *Nat. Commun.* 3 (2012) 1201.
- [40] D. Studer, H. Gnaegi, *J. Microsc.* 197 (2000) 94–100.
- [41] L.F. Drummy, R.J. Davis, D.L. Moore, M. Durstock, R.A. Vaia, J.W.P. Hsu, *Chem. Mater.* 23 (2010) 907–912.
- [42] K.T. Lee, W.H. Kan, L.F. Nazar, *J. Am. Chem. Soc.* 131 (2009) 6044–6045.
- [43] S. Park, K. Kameyama, T. Yao, *Electrochem. Solid State Lett.* 15 (2012) A49–A52.
- [44] M. Watanabe, F.I. Allen, *Ultramicroscopy* 113 (2012) 106–119.
- [45] B. Schaffer, G. Kothleitner, W. Grogger, *Ultramicroscopy* 106 (2006) 1129–1138.
- [46] B. Schaffer, W. Grogger, G. Kothleitner, *Ultramicroscopy* 102 (2004) 27–36.
- [47] P.G. Kotula, M.R. Keenan, J.R. Michael, *Microsc. Microanal.* 9 (2003) 1–17.
- [48] C.M. Parish, G.L. Brennecke, B.A. Tuttle, L.N. Brewer, *J. Am. Ceram. Soc.* 91 (2008) 3690–3697.
- [49] F.I. Allen, M. Watanabe, Z. Lee, N.P. Balsara, A.M. Minor, *Ultramicroscopy* 111 (2011) 239–244.
- [50] P. Conti, S. Zamponi, M. Giorgetti, M. Berrettoni, W.H. Smyrl, *Anal. Chem.* 82 (2010) 3629–3635.
- [51] M.R. Keenan, in: H.F. Grahn, P. Geladi (Eds.), *Techniques and Applications of Hyperspectral Image Analysis*, John Wiley & Sons Ltd, West Sussex, 2007, pp. 89–126.
- [52] M.R. Keenan, *Surf. Interface Anal.* 41 (2009) 79–87.
- [53] M.R. Keenan, P.G. Kotula, *Surf. Interface Anal.* 36 (2004) 203–212.
- [54] M.R. Keenan, P.G. Kotula, *Appl. Surf. Sci.* 231 (2004) 240–244.
- [55] P.G. Kotula, M.R. Keenan, *Microsc. Microanal.* 12 (2006) 538–544.
- [56] Y.-H. Pan, G. Vaughan, R. Brydson, A. Bleloch, M. Gass, K. Sader, A. Brown, *Ultramicroscopy* 110 (2010) 1020–1032.
- [57] K.W. Noh, Y. Liu, L. Sun, S.J. Dillon, *Ultramicroscopy* 116 (2012) 34–38.
- [58] H.M. Zheng, R.K. Smith, Y.W. Jun, C. Kisielowski, U. Dahmen, A.P. Alivisatos, *Science* 324 (2009) 1309–1312.
- [59] C.C. Ahn, *Transmission Electron Energy Loss Spectrometry in Materials Science and the EELS Atlas*, second ed., Wiley, Weinheim, Germany, 2004.
- [60] R.F. Egerton, *Electron Energy-loss Spectroscopy in the Electron Microscope*, second ed., Plenum Press, New York, 1996.
- [61] D.B. Williams, C.B. Carter, *Transmission Electron Microscopy: A Textbook for Materials Science*, Plenum Press, New York, 1996.
- [62] Y. Oriksa, T. Maeda, Y. Koyama, H. Murayama, K. Fukuda, H. Tanida, H. Arai, E. Matsubara, Y. Uchimoto, Z. Ogumi, *J. Am. Chem. Soc.* 135 (2013) 5497–5500.